Nanoscale Advances

ROYAL SOCIETY OF CHEMISTRY

PAPER

View Article Online
View Journal

Cite this: DOI: 10.1039/d4na00505h

L-cysteine capped MoS_2 QDs for dual-channel imaging and superior Fe^{3+} ion sensing in biological systems†

Vishakha Takhar, [a] Simranjit Singh, [b] Superb K. Misra [b] and Rupak Banerjee *[ac]

Received 17th June 2024
Accepted 11th September 2024

DOI: 10.1039/d4na00505h

rsc.li/nanoscale-advances

MoS_2 quantum dots (MQDs) with an average size of 1.9 ± 0.7 nm were synthesized using a microwave-assisted method. Absorbance studies confirmed characteristic transitions of MoS_2, with absorption humps at 260–280 nm and 300–330 nm, and a band gap of 3.6 ± 0.1 eV. Fluorescence emission studies showed dominant blue and some green emissions under 315 nm excitation, with an absolute quantum yield of ~9%. The MQDs exhibited fluorescence stability over time after repeated quenching cycles across various pH and media systems. *In vitro* toxicity tests indicated cytocompatibility, with around 80% cell survival at 1000 mg L^{-1}. Confocal imaging demonstrated significant uptake and vibrant fluorescence in cancerous and non-cancerous cell lines. The MQDs showed strong selectivity towards Fe^{3+} ions, with a detection limit of 27.61 ± 0.25 nM. Recovery rates for Fe^{3+} in phosphate buffer saline (PBS) and simulated body fluid (SBF) systems were >97% and >98%, respectively, with a relative standard deviation (RSD) within 3%, indicating precision. These findings suggest that MQDs have high potential for diagnostic applications involving Fe^{3+} detection due to their fluorescence stability, robustness, enhanced cell viability, and dual-channel imaging properties.

1. Introduction

The detection of heavy metal ions is crucial because of their ability to pose serious threats to both the environment and human health.[1,2] These ions can exert a wide variety of negative impacts on different human organs and systems. Adverse effects include cancer, renal damage, heart disease, and neurological issues that may arise from heavy metal exposure.[2] For this reason, precise heavy metal ion detection and monitoring are crucial to reducing their harmful effects on the environment and public health. In soft tissues of organisms, heavy metal ions can build up and have detrimental short and long-term consequences on different organs. In addition to being a source of physiological diseases and health hazards, heavy metals also play a significant role in the extensive pollution of the worldwide ecosystem.[3] Therefore, it is crucial to detect these heavy metal ions.

Fe^{3+} is a common element in natural settings and significantly impacts ecological balance and biological activities.[4] Fe^{3+} can operate as a catalyst in various chemical processes, changing the composition of natural systems and the activities of other contaminants. Fe^{3+} is involved in many processes, such as oxygen transport *via* hemoglobin, cellular metabolism, enzyme catalysis, RNA and DNA synthesis, and others. Also, Fe^{3+} can combine with organic molecules to produce complexes that can be hazardous to living things and interfere with essential biological processes. Excess of Fe^{3+} ions can cause conditions like hemochromatosis, Alzheimer's disease, Parkinson's disease, and harm to the lungs, pancreas, and heart. [5,6] Similarly, a deficiency of Fe^{3+} could lead to breathing problems, diabetes, and anemia, and iron levels need to be precisely monitored.[7] The normal serum iron levels for a healthy adult male typically range from 14.33 to 32.23 μM, while for a healthy adult female, the range is approximately 10.74 to 28.65 μM. In newborns, the serum iron concentration can range from 17.91 to 44.78 μM, and in children, from 8.96 to 21.50 μM. However, in pathological conditions, such as hemochromatosis, iron levels can exceed these normal ranges, leading to significant iron overload in the body. For neurodegenerative diseases, elevated iron levels in the brain can be substantial, with concentrations potentially reaching up to 10 μM in Alzheimer's disease and as high as 100 μM in Parkinson's disease.[8,9] To identify and treat disorders relating to the iron balance of the body, blood tests measuring serum ferritin levels, transferrin

[a]Department of Physics, Indian Institute of Technology Gandhinagar, Palaj, Gandhinagar, 382355, India. E-mail: rupakb@iitgn.ac.in

[b]Materials Engineering, Indian Institute of Technology Gandhinagar, Palaj, Gandhinagar, 382355, India

[c]K C Patel Centre for Sustainable Development, Indian Institute of Technology Gandhinagar, Palaj, Gandhinagar, 382355, India

† Electronic supplementary information (ESI) available. See DOI: https://doi.org/10.1039/d4na00505h

saturation, and total iron-binding capacity depend on precise Fe^{3+} ion detection.[10] Also, during chelation therapy or iron supplementation, Fe^{3+} level detection is imperative.[11] Besides medical conditions, Fe^{3+} ions are crucial as contrast agents in magnetic resonance imaging (MRI), ensuring their safety and effectiveness. Fe^{3+} poses potential health hazards by migrating and accumulating in environmental water systems through the food chain.

Researchers and environmental scientists may evaluate the overall stability of ecosystems, the quality of soil, and the health of water bodies by precisely monitoring and detecting Fe^{3+} levels.[7] The diagnosis and treatment of diseases associated with iron metabolism depend heavily on the accurate measurement of Fe^{3+} levels. Therefore, there is a critical need for selective and sensitive methods and probes to monitor and detect iron levels in biological systems, as well as in industrial and environmental samples. For the detection of these metal ions, several approaches are available, which include mass spectrometry,[12] calorimetry,[13] electrochemical,[10] and optical methods, including fluorescence photoluminescence (PL) quenching.[11] Among them, fluorescence-based PL detection is cost-effective and offers several advantages, such as high sensitivity, selectivity, real-time monitoring, and precise quantitative analysis.[14]

Quantum dots (QDs) are widely used in fluorescence-based detection techniques because of their exceptional fluorescence properties. QDs have also emerged as powerful tools for ion detection, leveraging their unique optical properties for sensitive and selective analysis. QDs have several benefits over conventional organic fluorophores, including resistance to photobleaching, a wide range of absorption spectra, narrow and adjustable emission spectra, and great photostability. However, there are inherent disadvantages with standard type II–VI semiconductor QDs, such as those made of cadmium telluride (CdTe) or cadmium selenide (CdSe). Long-term fluorescence experiments may find these QDs less useful due to their reduced photo-stability under extended irradiation. Furthermore, the existence of hazardous heavy metals such as cadmium in these QDs prompts worries regarding their influence on the environment and possible damage to biological systems.[15] Recent advances in the field of quantum dots, and particularly MoS_2 quantum dots, have demonstrated the possibility of resolving these issues.[16] The MoS_2 belonging to the family of transition metal dichalcogenides (TMDCs) have several benefits, including high photostability,[17] low toxicity, and biocompatibility, which makes them suitable for use in biological environments for heavy metal detection.[18] The distinct optical and electrical characteristics of MoS_2 quantum dots provide compelling evidence of the band gap transition.[19] While carbon dots can be used for Fe^{3+} sensing, MoS_2 quantum dots have several benefits that make their inclusion worthwhile. MoS_2 quantum dots are more sensitive and selective for Fe^{3+} detection due to their unique optical and electrical characteristics, which include strong photoluminescence, a large surface area, and good charge transfer abilities. According to these features, MoS_2 quantum dots can detect Fe^{3+} at considerably lower concentrations with greater precision than carbon dots. Furthermore, the variable band gaps of MoS_2 quantum dots allow for better control over the sensing properties. This is especially helpful in complicated biological or environmental samples with problematic interference. Therefore, MoS_2 quantum dots offer better performance in terms of sensitivity, selectivity, and overall dependability for Fe^{3+} sensing, making them a useful option for applications where these criteria are crucial.[20,21] While synthesis of these MoS_2 quantum dots (MQDs) is possible using various techniques, hydrothermal and microwave methods offer better control of the size, phase, and purity of the particles.[22–24] Among these, microwave synthesis offers faster and uniform heating, thereby reducing the overall synthesis time of the quantum dots.[25] MQDs have demonstrated enormous potential for technological application in a variety of fields. Due to their unique properties, MQDs offer remarkable versatility across several advanced fields. Through their strong and controllable photoluminescence, MQDs are used in optoelectronics to improve light emission efficiency and sensitivity in light-emitting diodes (LEDs) and photodetectors. In biomedical applications, their excellent biocompatibility and fluorescence make MQDs ideal for bio-imaging and drug delivery, allowing precise tracking of cells and targeted therapeutic interventions. MQDs are used in environmental applications to detect and eliminate contaminants, enhancing the effectiveness of ecological cleanup procedures. This is due to their large surface area and reactivity. Their catalytic qualities also make them useful in energy-related applications, such as hydrogen evolution processes, which advance the creation of sustainable energy technologies.[26]

This study presents a significant advancement in the synthesis of MoS_2 quantum dots through a microwave-assisted method, which notably contrasts with the commonly used, but time consuming, hydrothermal method. Our method achieves rapid synthesis in just 1 hour, resulting in quantum dots with a very small size and high biocompatibility. The MQDs produced are small in size (~2 nm), highly biocompatible, and exhibit strong blue and green fluorescence when excited under UV light. We thoroughly analyzed the stability of the MQDs before conducting *in vitro* studies, where their cytotoxicity was assessed on both cancerous (SK-BR-3) and non-cancerous (RPE-1) cell lines, followed by bioimaging studies using blue and green channels under UV excitation. The MQDs demonstrated excellent selectivity and high sensitivity toward Fe^{3+} ions, with a low detection limit of 27.61 ± 0.25 nM, highlighting their potential for application in environmental sensing and biomedical diagnostics. This study presents a significant improvement over traditional methods, offering a faster and more effective approach to MQD synthesis.

2. Materials and methods

2.1 Materials

Sodium molybdate dihydrate, hydrochloric acid, sodium hydroxide and L-cysteine, and mowiol mounting media were purchased from Merck. DMEM, Modified McCoy's 5 A media, and FBS were procured from Gibco while 3-(4,5-dimethylthiazolyl-2)-2,5-diphenyltetrazolium bromide (MTT), 4% paraformaldehyde, phosphate buffer saline (PBS) (pH 7.4), and

penicillin-streptomycin antibody solution were supplied by HiMedia. Additionally, ethanol, acetone, DMSO, and sodium molybdate dihydrate were used in the research and were purchased from Merck. Calcium chloride ($CaCl_2$), copper chloride ($CuCl_2$), cesium chloride (CsCl), lead chloride ($PbCl_2$), manganese chloride ($MnCl_2$), nickel chloride ($NiCl_2$), antimony chloride ($SbCl_3$), zinc chloride ($ZnCl_2$), silver chloride (AgCl), mercury chloride ($HgCl_2$), iron chloride ($FeCl_2$), and iron chloride ($FeCl_3$) were purchased from Sigma-Aldrich. Neodymium chloride ($NdCl_3$), thulium chloride ($TmCl_3$), yttrium chloride (YCl_3), and ytterbium chloride ($YbCl_3$) were procured from Alfa Aesar. The SK-BR-3 and RPE-1 cell lines were procured from the National Centre for Cell Science (NCCS), Pune.

2.2 Synthesis of MoS_2 quantum dots

The synthesis of MoS_2 quantum dots was accomplished using a microwave-assisted method. The pH of the solution containing 0.25 g of sodium molybdate dihydrate ($Na_2MoO_4 \cdot 2H_2O$) in ultrapure water was adjusted to 6.5 with the help of 0.1 M HCl. After 15 min of constant stirring, a solution containing 0.5 g of L-cysteine in 50 mL water was added dropwise to the above solution. This final solution mixture was then transferred to microwave vessels for microwave irradiation (200 °C for 1.5 h, PerkinElmer, Titan MPS). The supernatant containing MoS_2 quantum dots was collected by centrifugation at 13 000 rpm for 15 min. The supernatant was filtered through 0.22 μm and dried at 60 °C to obtain MQDs. The formation of these quantum dots could be explained through the equations below:

$$HSCH_2CHNH_2COOH + H_2O \rightarrow CH_3COCOOH + NH_3 + H_2S \quad (1)$$

$$4MoO_4^{2-} + 9H_2S + 6CH_3COCOOH \rightarrow 4MoS_2 + SO_4^{2-} + 6CH_3COCOO^- + 12H_2O \quad (2)$$

2.3 Characterization

The morphology and size distribution of the MQDs were measured using Transmission electron microscopy (TEM) (FEI, Themis 300) and atomic field microscopy (AFM) (Bruker Nano wizard Sense AFM). X-ray diffraction (XRD) (CuK_α, SmartLab, Rigaku Corp., Japan) and Raman measurements (532 nm, Labram HR800 Evolution, Horiba Jobin Yvon) were conducted to determine the crystalline phases (2θ range of 10°–90°) and vibrational modes of the MQDs. The optical properties of the MQDs were measured using UV-Vis spectroscopy (Lambda 365, PerkinElmer) from 200 to 600 nm and Fluorescence spectroscopy (FP-8300, Jasco) at an excitation of 315 nm. The band gap was calculated using Tauc's equation (eqn (3)).[27] The quantum yield measurements were conducted using an integrated sphere in a fluorescence spectrophotometer (Fluorolog, Horiba). To assess the effect of Fe^{3+} ions on the MQDs, Fourier Transform Infrared Spectroscopy (FTIR) was conducted in ATR mode (Perkin Elmer-Spectrum two), and the suspension stability and hydrodynamic size was determined using Zeta potential measurements dynamic light scattering (DLS) (Nano ZS, Malvern Instruments).

$$\alpha h\nu = B(h\nu - E_g)^n \quad (3)$$

where E_g is the bandgap, $h\nu$ is the photon energy, B is the constant, $n = 1/2$, and α is the absorption coefficient.

2.4 Cell culture studies

The cell culture studies were performed on a cancerous cell line SK-BR-3 (human breast cancer cell line) and a non-cancerous cell line RPE-1 (human retinal cell line). The SK-BR-3 cells were cultured in modified McCoy's A media, while the RPE-1 were grown in DMEM with 10% FBS and 1% antibiotic solution (penicillin–streptomycin) as the supplements. The cells were incubated and cultured at 37 °C under 5% CO_2 flow under humid conditions.

2.4.1 Cell toxicity studies. The cell toxicity experiments were conducted by seeding 100 μL containing 1×10^4 cells in each well of a 96-well plate with complete media. After the cells attained their respective morphology, the media was replaced with treatment samples of different concentrations (2.5 μg mL^{-1} and 2500 μg mL^{-1}) prepared in the respective media for the cell line. After 24 h of treatment, the cells were washed using PBS to remove leftover treatment samples. Following, 100 μL of MTT dye solution of 500 μg mL^{-1} concentration was added to each well for 3 h of incubation. Subsequently, the dye solution was removed, and 100 μL of DMSO was added to each well before recording the absorbance value at 570 nm in a plate reader (Biotek Cytation 5).

2.4.2 Cellular imaging studies. Uptake and imaging studies on MQDs were conducted using a confocal microscope (Leica TCS SP8). To facilitate imaging, 1×10^5 cells suspended in complete media were seeded over a glass coverslip placed in 12 well plate. The media was replaced by 100 μg mL^{-1} of MoS_2 QD suspension prepared in the media. After 24 h of incubation, the cells were washed with PBS to remove excess MQD particles. Afterward, cells were fixed using a 4% PFA solution and mounted onto glass slides with the help of mounting media. Finally, imaging was carried out using a 405 nm confocal laser, which was able to capture separate channels for green emission (520–560 nm) and blue emission (420–500 nm). The obtained Z-stack pictures were then thoroughly analyzed with Image-J software.

2.5 Ion selectivity and sensitivity studies

The ion sensing studies were conducted using a fluorescence spectrophotometer by observing the changes in the intensity of the PL emission spectra of the MQDs. For the selectivity studies, 50 μM concentration of the quantum dots and 500 μM different metal ions were mixed in a 1 : 1 volume ratio, and the emission spectra were recorded from 325 to 650 nm at the excitation wavelength of 315 nm. For the comparative studies, a range of metal ions, including Ca^{2+}, Cu^{2+}, Cs^{3+}, Pb^{2+}, Mn^{2+}, Ni^{2+}, Sb^{3+}, Zn^{2+}, Ag^+, Hg^{3+}, Nd^{3+}, Tm^{3+}, Y^{3+}, Yb^{3+}, Fe^{2+} and Fe^{3+} were chosen to figure out the metal ion for which the MQDs have

a maximum affinity. Since the maximum change in the PL intensity was observed in the case of Fe^{3+} ions, it was selected for further studies. Similarly, for the sensitivity experiment, different concentrations of the selected Fe^{3+} ion from 0 μM to 5000 μM were varied, and the changes in the PL intensity were measured. The limit of detection (LOD) and limit of quantification (LOQ) for Fe^{3+} ions were calculated using the following equation[28]

$$\mathrm{LOD} = \frac{3\sigma}{s} \quad (4)$$

$$\mathrm{LOQ} = \frac{10\sigma}{s} \quad (5)$$

where σ is the standard deviation, and s is the slope of the calibration.

2.6 Statistical analysis

The statistical analysis of the data was carried out using GraphPad Prism software. The mean, standard deviation, and multiple analyses were performed using the one-way ANOVA test in a minimum of three trials. Statistics were considered statistically significant when the p-value was less than 0.05 (****$p < 0.0001$; ***$p < 0.001$; **$p < 0.01$; *$p \leq 0.05$).

3. Results and discussion

3.1 Characterisation of MQDs

Fig. 1(a) reveals the spherical morphology of MQDs obtained from AFM along with the height profiling in Fig. 1(b) and S1 (ESI†). The TEM image, along with the statistical particle size distribution, are shown in Fig. 1(c) and (d), respectively. The average size of MQDs obtained from TEM was found to be 1.9 ± 0.7 nm, which agrees with the AFM height profiling data. The HRTEM image shown in the inset of Fig. 1(c) reveals the planes of MQDs having lattice spacing of 0.22 nm, which corresponds to the (103) plane of MoS_2. The TEM measurements, as illustrated in Fig. S2 (ESI†), confirm a well-dispersed distribution of MQDs. The resolution of 0.5 nm in the size distribution is corroborated by Fig. S2 (ESI†), which shows particle size variations from approximately 0.8 nm to 2.3 nm. Additionally, the Dynamic Light Scattering (DLS) results for the MoS_2 quantum dots indicate an average size of ~40 nm, as illustrated in Fig. S3 (ESI†). This size measurement reflects the overall hydrodynamic diameter of the quantum dots in solution, providing insight into their dispersion and stability. The phase and the planes of MQDs were further analyzed using XRD as shown in Fig. 1(e). The XRD spectrum reveals the 1T phase of the MQDs consisting of (002), (100), (101), (103), (006), (106), and (200) peaks indexing with the planes of MoS_2 (JCPDS: 00-009-0432).[29] The crystallite size corresponding to the (002) plane was determined using the Scherrer formula [29] and found to be 6.71 nm. The purity of the 1T phase of MoS_2 was further confirmed through Raman spectroscopy, as shown in Fig. S4 (ESI†). The Raman spectrum of MoS_2 quantum dots revealed peaks at 158 cm^{-1} (J_1), 226 cm^{-1} (J_2), 285 cm^{-1} (E_{1g}), 332 cm^{-1} (J_3), and 415 cm^{-1} (A_{1g}), which are indicative of the specific vibrational modes characteristic of the 1T phase of MoS_2.[30] The presence of Mo–S could be verified by the presence of a 465 cm^{-1} peak in the FTIR spectra. Moreover, the presence of the amine group can be attributed to wavenumbers 3374 cm^{-1} and 1567 cm^{-1} representing N–H stretching and in-plane N–H stretching, while the 1410 cm^{-1} is due to the carboxyl group, as seen from Fig. S5 (ESI†). The absorbance investigations were carried out before examining the fluorescence characteristics of MQDs. The UV-Vis absorption of MQDs is shown in Fig. 1(f), with absorption humps ranging from 260 to 280 nm and 300 nm to 330 nm, which can be attributed to the characteristic transitions of MQDs. Also, from Tauc plot in the inset of Fig. 1(f), the band gap of the MQDs was determined using eqn (3) and was found to be 3.6 ± 0.1 eV, The elemental mapping was performed (see Fig. S6 in ESI†) demonstrating uniform distribution of sulfur (S) and molybdenum (Mo) throughout the sample, substantiating the existence of MoS_2 quantum dots. This is further supported by the accompanying energy-dispersive spectroscopy (EDS) data, which displays Mo and S peaks and an elemental ratio of around 59.1 : 40.9, which is in accordance with the predicted stoichiometry of MoS_2.

3.2 Fluorescence properties of MQDs

The absorbance spectra of MQDs fall in the UV range. An image of synthesized MQDs suspension was captured under UV illumination, as shown in the inset of Fig. 2(a), showcasing their distinct characteristic blue color emission. Subsequently, wavelength-dependent emission measurements were conducted to verify the excitation wavelength generating the highest emission. The most intense emission was observed at 405 nm (blue), with a minor emission at 530 nm (green) when excited at 315 nm, as shown in Fig. 2(a), leading to the selection of this wavelength for further studies. Moreover, when the wavelength was changed from 315 to 440 nm, the emission of the MQDs showed a red shift from 405 nm to 490 nm with a significant decrease in the overall emission intensity (Fig. 2(a)).[31] The quantum yield (QY) of MQDs was measured using an integrated sphere setup, yielding a value of 8.95 ± 0.02%. This QY reflects the efficiency of photon emission upon excitation, which is crucial for applications such as ion sensing and bioimaging. Despite being moderate, this QY is adequate for generating sharp and detailed images in biomedical contexts, where the low toxicity and biocompatibility of MQDs make them excellent imaging agents. In ion sensing, the tunable fluorescence of MQDs allows for the detection of specific metal ions, with potential enhancements through surface modifications. Additionally, a concentration-dependent study (between 1000 and 1.25 mg L^{-1}) revealed the lowest detectable emission for the MQD concentration of 1.25 mg L^{-1}. Based on the emission features shown by the fluorescence image in Fig. 2(b) and its inset, a MQD concentration of 100 mg L^{-1} was chosen for subsequent studies.

3.3 Stability studies

To conduct the applicability investigations, 100 mg L^{-1} MQDs were suspended in various solvents (ultrapure water, PBS,

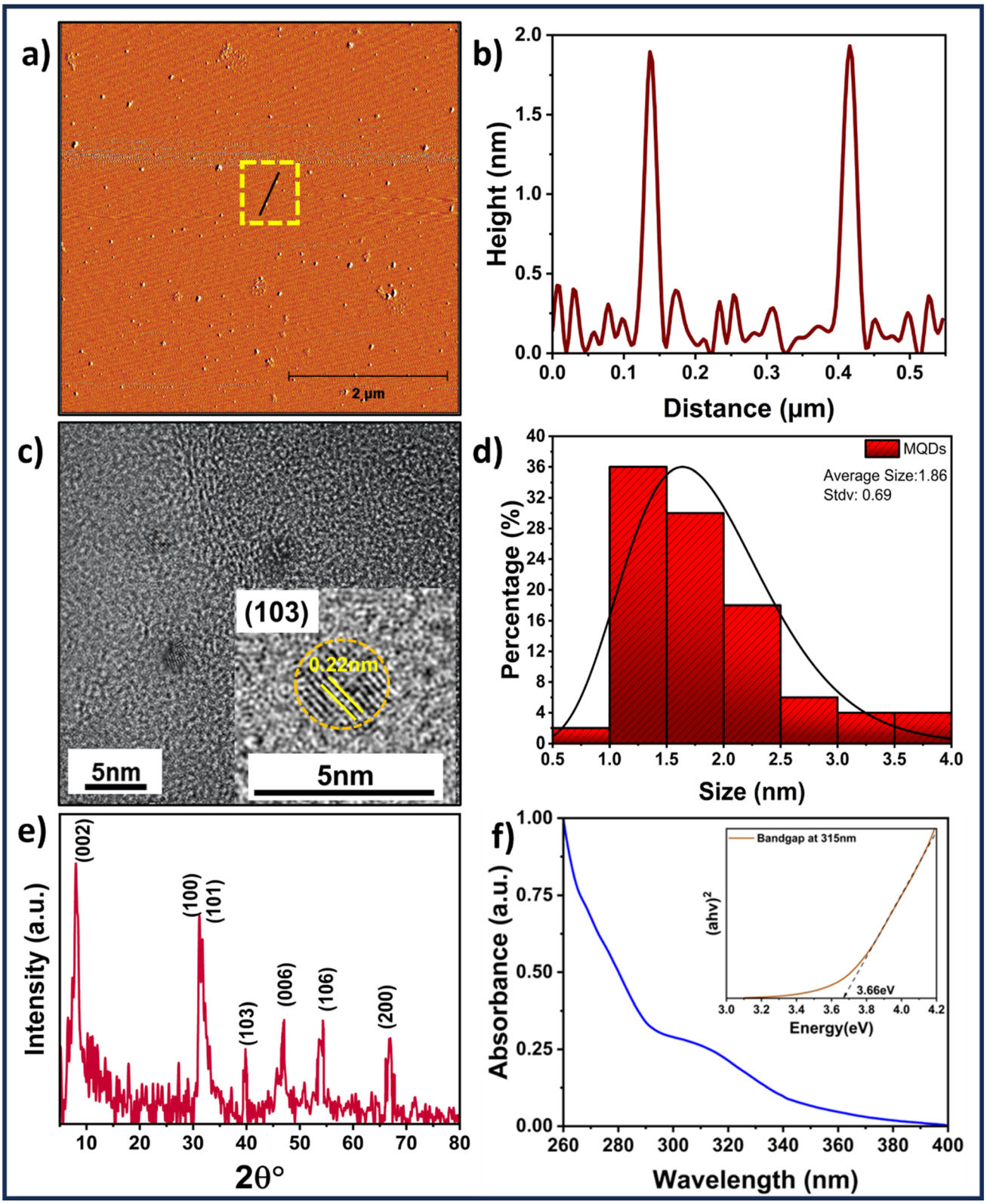

Fig. 1 (a) AFM image of MQDs along with the (b) height profile of the selected region shown in broken lines, (c) TEM images of MQDs with a high-resolution image of the MQD in the inset revealing its (103) plane, (d) size distribution of MQDs calculated from the TEM ($n = 100$), (e) XRD profile of the MQDs and (f) UV-Vis spectrum along with Tauc plot depicting the band gap of MQDs in the inset.

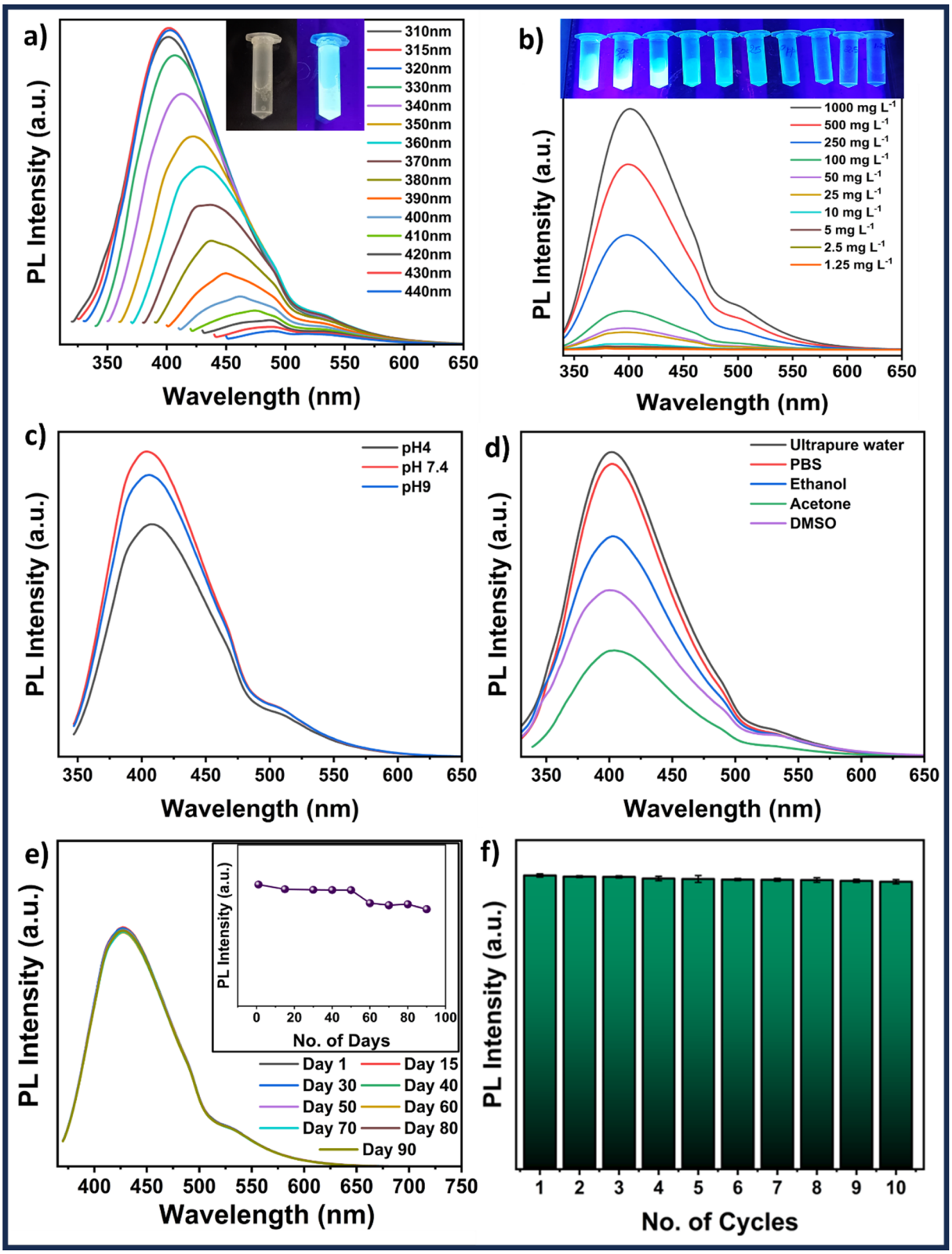

Fig. 2 (a) Wavelength-dependent fluorescence spectra of MQDs with varying excitation wavelength (from 310 to 440 nm) along with the inset image depicting the characteristic blue color of MQDs under UV illumination, shown alongside the MQD suspension without UV illumination. (b) Concentration-dependent fluorescence spectra and inset images of MQDs under UV illuminator (from 1.25 mg L^{-1} to 1000 mg L^{-1}), (c) fluorescence spectra of MQDs in different pH systems (concentration 100 mg L^{-1}), (d) solvent-dependent fluorescence spectra of MQDs (concentration 100 mg L^{-1}), (e) fluorescence stability of MQDs tested over 90 days at a concentration of 100 mg L^{-1}, and (f) bar graphs representing quenching studies of MQDs for 10 cycles after exposure to UV illumination taken at a time interval of 5 min.

ethanol, acetone, and DMSO) and pH (4, 7.4, and 9) systems. Fig. 2(d) verifies that the MQDs have emission in all the solvents used in the study; however, ultrapure water and PBS had the highest intensity of emission, followed by ethanol, acetone, and DMSO. A similar study that varied the pH revealed some fluctuation between pH 4 and pH 9 (Fig. 2(c)). The highest emission intensity was attained at pH 7.4, followed by pH 9 and pH 4. The PL emission spectra of MQDs were fitted for various suspension systems at an excitation wavelength of 315 nm. The fitted peak positions are summarized in Table S1 (ESI†), while the fitting curves for all samples are presented in Fig. S7 (ESI†). The analysis reveals three primary emission peaks: the first, around 394–402 nm, corresponds to band-edge emission, which is linked to quantum confinement effects and reflects the structural integrity of the QDs. The second peak observed between 430–458 nm, is associated with defect states such as sulfur vacancies, indicating variations in the defect density or nature, particularly in different organic solvents. The third peak, occurring between 504–543 nm, is related to surface state emissions, which are highly sensitive to the surrounding environment, with significant shifts observed in acetone, suggesting strong solvent-QD surface interactions. These peak values and their observed shifts are consistent with existing literature, where band-edge emissions typically fall within the 400–450 nm range, defect-related emissions are reported around 450–500 nm, and surface state emissions are found between 500–550 nm. The variations in peak positions across different media suggest that while the core structure of MoS_2 QDs remains stable, their surface properties are more susceptible to environmental changes. This combination of stability and tunable surface chemistry highlights the potential of MoS_2 QDs for various applications, especially those involving significant surface interactions.[32] Fluorescence studies were carried out at various time intervals up to 90 days to determine the stability of the MQDs. The results shown in Fig. 2(e) demonstrate the excellent emission stability of MQDs by displaying that the fluorescence intensities are invariable over 50 days, decrease slightly over the next 20 days, and stabilize at 90 days. A similar experiment was conducted to investigate the quenching characteristics of the MQDs. In this case, the particles were continuously exposed to ultraviolet (UV) illumination, and the emission was monitored every five minutes for ten consecutive cycles, as demonstrated in Fig. 2(f). The excellent photostability and low quenching of MQDs are displayed by the minimal decrease in fluorescence intensity. Thus, these studies demonstrate the robustness and stability of MQDs, which makes them outstanding choices for environmental and biological applications.

3.4 Cell viability and imaging studies

The cell viability and imaging were carried out on RPE-1 (non-cancerous) and SK-BR-3 cell lines (cancerous). These cell lines were deliberately selected to verify the robustness of the MQDs among different cell lines and conditions. The objective was to evaluate the efficacy of the particles in different cellular environments. Cancerous cells, characterized by lower pH levels,[33] and non-cancerous cells with neutral pH were selected to represent distinct environments. From Fig. 3, it can be interpreted that the cell viability of both the cell lines remains more than 75% even at a high concentration of 1000 μg L^{-1}, thus representing the cytocompatibility of the MQDs. The synthesis process involving L-cysteine contributes significantly to the remarkably low toxicity observed in MQDs. L-Cysteine, a naturally occurring amino acid known for its biocompatibility and antioxidative properties, forms a stable coating layer on the surface of QDs, acting as a protective barrier against cytotoxicity. This surface modification enhances the dispersibility and stability of MQDs in physiological environments while reducing oxidative stress and preventing cellular damage. Moreover, L-cysteine facilitates interactions with biomolecules and cellular components, promoting cellular uptake and intracellular trafficking of MQDs without inducing significant cytotoxic effects.[34,35]

L-Cysteine capped MQDs were assessed for their antioxidative qualities using a DPPH (2,2-diphenyl-1-picrylhydrazyl) radical scavenging experiment. By measuring the decrease in absorbance at 517 nm, which indicates the reduction of the DPPH radical, the DPPH test is a well-researched technique for evaluating the ability of a compound to scavenge free radicals. As depicted in Fig. S8(a) in the ESI,† the percentage of DPPH inhibition increased with the concentration of MQDs. The highest inhibition was observed at 1000 mg L^{-1}, indicating strong radical scavenging activity. The concentration-dependent increase in DPPH inhibition suggests that the L-cysteine-capped MQDs possess significant antioxidative properties. Simultaneously, when the quantity of MQDs increased, there was a discernible decrease in absorbance as indicated by the UV-Vis absorption spectra of the DPPH solution. The gradual reduction in absorbance intensity, as seen in Fig. S8(b) in the ESI,† confirms the dose-dependent quenching of the DPPH radical by the MQDs. The dose-dependent quenching of the DPPH radical by the MQDs is confirmed by the steady drop in absorbance intensity, as shown in Fig. S8(b) in the ESI.†

The cellular imaging of MQDs was conducted on cancerous and non-cancerous cell lines. The MQDs were incubated for 24 h allowing both the cell lines to uptake these particles.

Once the cellular uptake is achieved, the imaging of both SK-BR-3 and RPE-1 could be accomplished through confocal microscopy as illustrated in the schematic Fig. 4(a). Fig. 4(b) and (c) represent confocal Z-stack images of SK-BR-3 cells, while Fig. 4(d) and (e) represent RPE-1 cell lines in blue and green channels, respectively, under UV excitation. These images were obtained after removing the background autofluorescence from each cell line depicted in Fig. S9 of the ESI.† The presence of L-cysteine on the MQDs not only acts as a capping agent that stabilizes the quantum dots in the suspensions but rather also plays a crucial role in increasing biocompatibility (Fig. 3) and aiding in cellular uptake.[35] Previous studies have shown that the cellular uptake of L-cysteine-capped QDs involves interactions with cell membranes, allowing them to enter the cells efficiently and enhancing cellular uptake.[36]

The imaging studies indicate the dual-channel imaging application of the MQDs when excited with UV illumination.

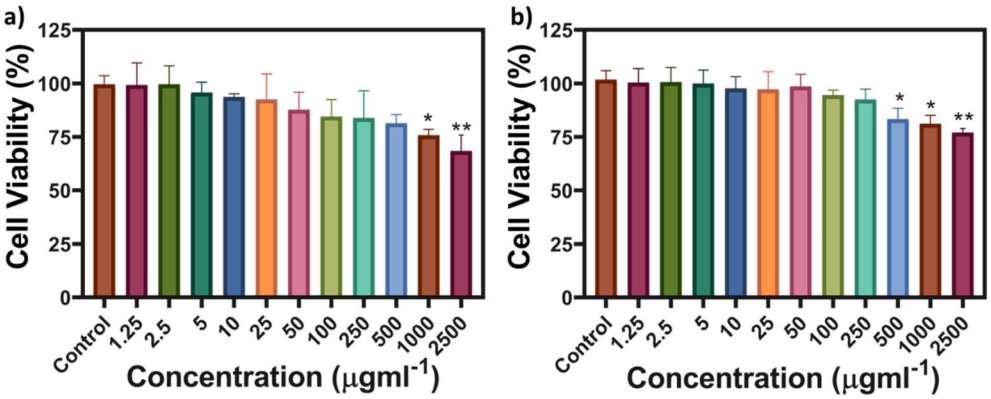

Fig. 3 MTT-based cell viability of (a) SK-BR-3 and (b) RPE-1 cell lines from concentrations of MQDs ranging from 1.25 to 2500 μg L^{-1}.

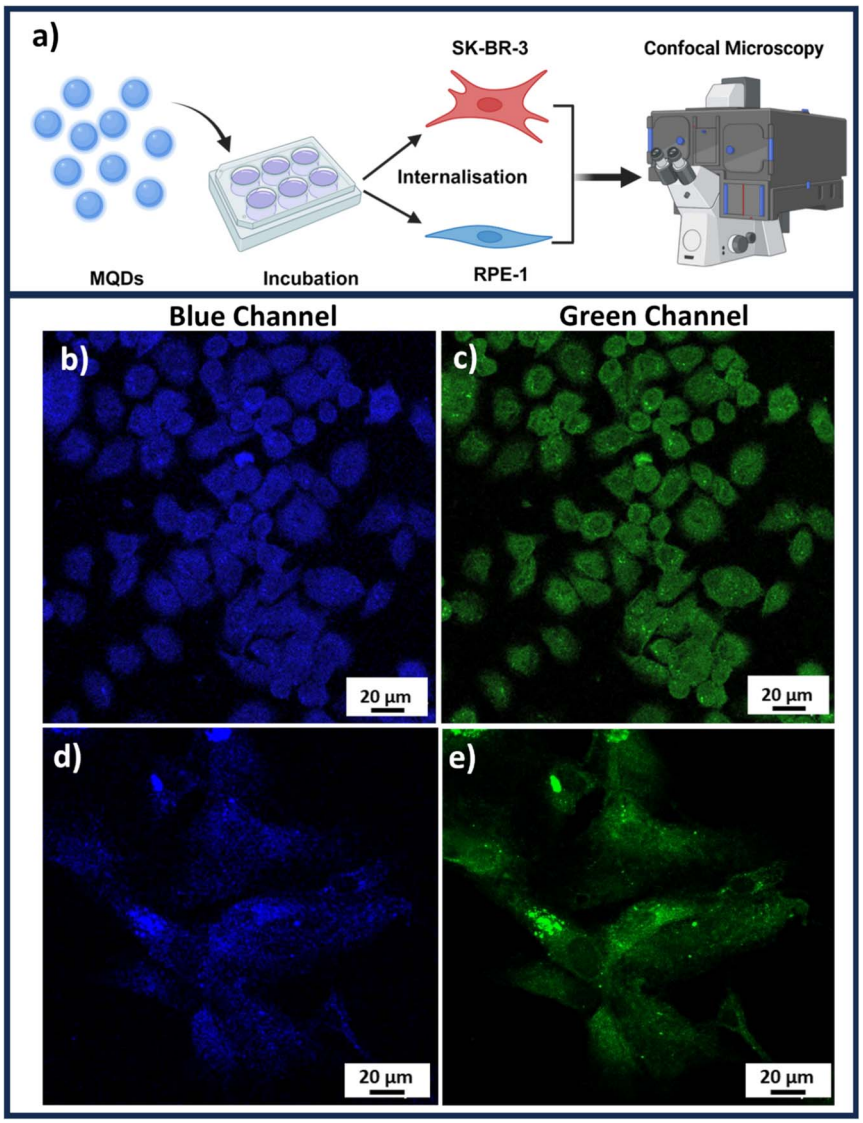

Fig. 4 (a) Overall schematic of confocal-based cellular imaging of MQDs, confocal images of SK-BR-3 in (b) blue channel, (c) green channel, and RPE-1 in (d) blue channel and (e) green channel under UV excitation (concentration: 100 μg mL^{-1}).

From Fig. 4(b)–(e), it is observed that the MQDs were found uniformly around the cytoplasm and nucleus of both the cancerous and non-cancerous cell lines. However, interestingly it was observed that the cellular uptake of MQDs demonstrates higher fluorescence in both blue and green channels for SK-BR-3 compared to the RPE-1. This could be attributed to the higher rate of metabolism for cancerous cells compared to non-cancerous cells, which leads to higher and rapid uptake of MQDs in cancerous cell lines.[37]

The observed difference in MQD uptake efficiency may explain the distinct cytocompatibility trends in Fig. 3, where the higher metabolic activity in cancerous cells leads to a more robust interaction with the MQDs. This increased cellular uptake in SK-BR-3 cells suggests greater potential for MQDs in targeted imaging or therapeutic applications, particularly in cancer cells where rapid internalization is advantageous. The combination of high cytocompatibility (Fig. 3) and effective cellular imaging (Fig. 4) highlights MQDs as promising tools for biomedical applications, especially in cancer detection and treatment. The improved biocompatibility and cellular absorption, facilitated by L-cysteine, further support the utility of MQDs in these fields, with their low toxicity and effective cellular interaction being crucial for their application.

3.5 Ion sensing and applications in biological media

The ion sensing was analyzed by studying the decrease in the fluorescence intensity of MQDs when exposed to heavy metal ions. The addition of specific ions results in attenuation of the characteristic blue color of the MQDs under UV irradiation. For every experiment, the excitation wavelength is set at 315 nm, and the maximum emission peak occurs at about 405 nm. Cross-influence from scattered excitation light is efficiently minimized by keeping an interval of around 90 nm between the maximal emission wavelength and the excitation. For comparative selectivity studies, a range of metal ions, including Ca^{2+}, Cu^{2+}, Cs^{3+}, Pb^{2+}, Mn^{2+}, Ni^{2+}, Sb^{3+}, Zn^{2+}, Ag^{+}, Hg^{3+}, Nd^{3+}, Tm^{3+}, Y^{3+}, Yb^{3+}, Fe^{2+} and Fe^{3+} were chosen to figure out the metal ion for which the MQDs have a maximum affinity. Fig. 5(a) depicted that the maximum change in the fluorescence intensity was observed in the case of Fe^{3+} ions, thus proving to be most responsive towards MQDs. Hence, using this phenomenon, a room-temperature fluorescent MQDs–Fe^{3+} detection system is developed and studied in detail for further studies. The response time optimization of the MQDs was conducted by recording the fluorescence of MQDs at the time interval of every 1 min initially after the addition of the ions. Fig. 5(b) demonstrates a fast response of MQDs (1 s) after the addition of all the ions (Ca^{2+}, $Fe^{2+,}$ and Fe^{3+}), which also remained consistently stable for 15 min. For the sensitivity experiment, Fe^{3+} aqueous solution of different concentrations (0 μM to 5000 μM) was added to the MQDs suspension. Notably, this quenching in the fluorescence intensity increases with increasing Fe^{3+} concentration, which can be observed in Fig. 5(c). When the concentration of Fe^{3+} reaches 1250 μmol, the fluorescence almost disappears (Fig. 5(c)). At lower concentrations of Fe^{3+}, the fluorescence intensity exhibits linear behavior (Fig. 5(d)). In the low Fe^{3+} concentration range of 0–500 nmol, enhanced linearity is seen, and the correlation between fluorescence intensity and Fe^{3+} concentration is impressive ($R^2 = 0.9954$) (Fig. 5(d)). Additionally, the fluorescence quenching process within the linear region is more accurately described by the Stern–Volmer function (eqn (6)).[38] For Fe^{3+} concentrations ranging from 0–500 nmol, the quenching constant K_{SV} is determined to be 8.788×10^4 M^{-1}. However, the overall behavior within the range of 0–5000 μM can be comprehensively understood using the exponential function (Fig. S10 in ESI†). This function accurately captures fluorescence quenching, even when linearity is not evident ($R^2 = 0.99723$). The limit of detection (LOD) and limit of quantification (LOQ) calculated from eqn (4) and (5) reaches down to 27.61 ± 0.25 nmol and 92.03 ± 0.32 nmol, respectively. Furthermore,

$$\frac{F_0}{F} = 1 + K_{SV} C[Fe^{3+}] \quad (6)$$

where F_0 is the fluorescence intensity at 315 nm and K_{SV} is the quenching constant.

To evaluate the potential application of MQDs, biological media such as phosphate buffer saline (PBS) and simulated body fluid (SBF) were used. PBS was procured from HiMedia, and SBF was prepared using the precursor formulation listed in Table S2.†[39] Fe^{3+} solutions with concentrations ranging from 0 μM to 2500 μM were prepared in both SBF and PBS and subsequently added to the MQD suspensions. Notably, the quenching of fluorescence intensity increased with the rising Fe^{3+} concentration, as depicted in Fig. 6. When the Fe^{3+} concentration reached 2500 μM, the fluorescence was almost entirely quenched (Fig. 6). The recovery of Fe^{3+} ions in the SBF and PBS systems was assessed using the standard addition method, with results summarized in Table S3 (see ESI†). The recovery rates for Fe^{3+} in PBS and SBF samples were found to be >97% and >98%, respectively. The relative standard deviation (RSD) was within 3%, indicating excellent precision for Fe^{3+} detection. These findings demonstrate that microwave-synthesized MoS_2 quantum dots are effective for detecting Fe^{3+} in biological samples.

3.6 Mechanism of Fe^{3+} ion sensing

A schematic revealing how the presence of Fe^{3+} ions might reduce the fluorescence of MQDs is shown in Fig. 7(a). As seen in Fig. 7(b), the presence of negatively charged sulfur and carboxylic groups on the surface of MQDs results in a zeta potential of −55 mV in the absence of Fe^{3+} ions. L-cysteine assists in preserving the stability of MQD suspension through this negative zeta potential. The increase in the zeta potential to +13 mV, as shown in Fig. 7(b), indicates that adding Fe^{3+} ions causes them to be drawn to the surface of the MQDs. This shift signifies the build-up of Fe^{3+} ions on the negatively charged MQD surface, which causes the surface to become positively charged. This method is appropriate for detecting Fe^{3+} ions because it validates the electrostatic contact between Fe^{3+} ions and the MQD surface, which results in fluorescence quenching.[40] The dynamic and static quenching mechanisms could be identified by the TRPL measurements. The individual fitted

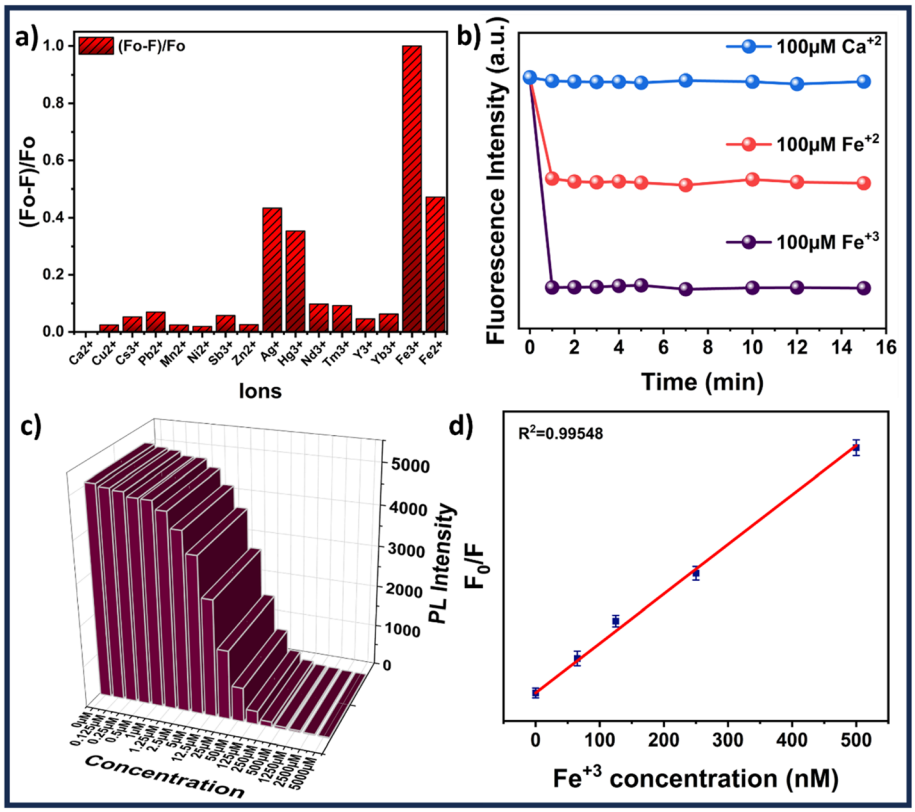

Fig. 5 (a) Bar graph illustrating the fluorescence-based selectivity response of MQDs over a series of different heavy metal ions, (b) the response time optimization of the MQDs after the addition of Fe^{3+} ions, (c) Fe^{3+} concentration-dependent fluorescence quenching study of MQDs, (d) linear function describing fluorescence quenching by Fe^{3+} ions (concentration range 0 nM to 500 nM).

curves for each of the three samples – (i) pristine MQDs, (ii) MQD with 100 μM Fe^{3+} ions, and (iii) MQD with 5000 μM Fe^{3+} ions, as well as the comparative related TRPL investigations, are shown in Fig. S11.† Using eqn (7), the exciton lifetime in the TRPL measurement was fitted, revealing tri-exponential decay and the associated lifetime for each decay (τ_1, τ_2, and τ_3) (Table S4 in ESI†). According to this tri-exponential decay spectrum, there are three different kinds of PL emission centers. The three decay lifetimes did not initially alter significantly when the concentration of Fe^{3+} ions increased from 0 to 5000 μM.

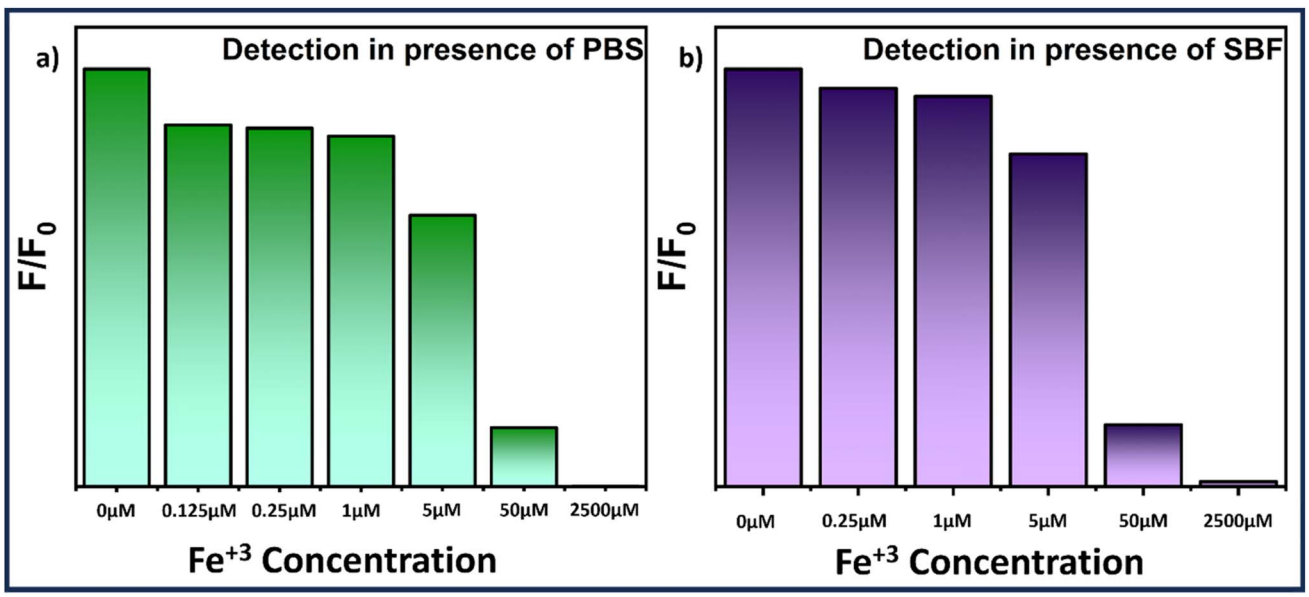

Fig. 6 Bar graph illustrating the Fe^{3+} concentration-dependent fluorescence quenching study of MQDs in (a) PBS and (b) SBF solution.

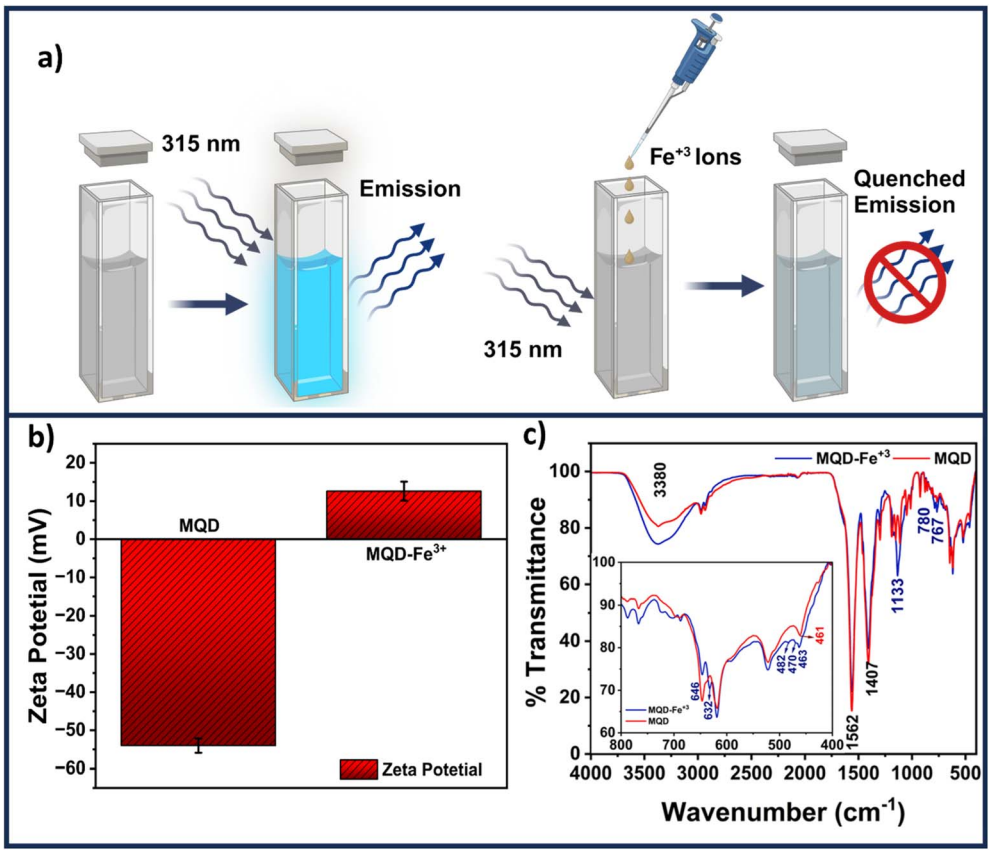

Fig. 7 (a) Schematic representing the mechanism of fluorescence quenching of MQDs in the presence of Fe^{3+} ions, (b) zeta potential measurements of MQDs and MQD with Fe^{3+} ions in ultrapure water, (c) FTIR spectrum of MQDs and MQD with Fe^{3+} ions.

Additionally, the relative change in fluorescence lifespan (τ_0/τ_{av}) was computed and found to vary from 1 (for bare MQDs) to 0.952 (for 5000 Fe^{3+} with MQDs). The relatively minor variation in τ_{av} might be associated with the trap-state emission of MQDs due to defects in the surface caused by the ion-binding effect. This may infer that the quenching of PL emission was entirely static.[40] The size of MQDs has a significant impact on their fluorescence lifespan. Shorter fluorescence lifetimes are caused by changes in the electronic structure of MQDs brought about by quantum confinement phenomena as they get smaller. The main cause of this shortening is the higher frequency of non-radiative recombination processes found in smaller MQDs. Smaller quantum dots have a greater surface-to-volume ratio, which increases the density of surface states. This can trap excitons and provide paths for non-radiative decay. These surface states cause smaller MQDs to display a greater rate of non-radiative recombination, which further shortens their fluorescence lifespan. Consequently, differences in MQD size can cause significant variations in their fluorescence lifespan, which can affect how well they work in applications that need exact optical properties.

$$y = Ae^{-\frac{t}{\tau_1}} + Be^{-\frac{t}{\tau_2}} + Ce^{-\frac{t}{\tau_3}} \quad (7)$$

The FTIR spectra shown in Fig. 7(c) offer a detailed understanding of the static interaction between Fe^{3+} ions and MQDs through surface adsorption. The broad peak at 3380 cm^{-1}, corresponding to hydroxyl (–OH) stretching vibrations, narrows and slightly shifts after Fe^{3+} ions are introduced, indicating that these ions are adsorbed onto the surface of MQDs, likely interacting with the –OH groups. The peak at 1562 cm^{-1}, attributed to carbonyl (C=O) stretching from carboxylic acid or amide groups, also exhibits a minor shift, suggesting that Fe^{3+} ions are binding to these electron-rich groups on the MQD surface, forming stable complexes.[41–43] Similarly, the C–N stretching or bending vibration at 1407 cm^{-1}, characteristic of amine or amide groups, shows narrowing after the addition of Fe^{3+}, reflecting the interaction of these ions with nitrogen-containing functional groups repeated.[24] This interaction is a result of Fe^{3+} ions being adsorbed onto the surface, leading to the formation of non-fluorescent complexes that are critical for the detection mechanism.[44] The peak at 1133 cm^{-1}, associated with C–O stretching vibrations from alcohols, ethers, or carboxylic acids, also undergoes narrowing, indicating that Fe^{3+} ions are interacting with these oxygen-containing groups on the MQD surface. The Mo–S stretching vibration at 461 cm^{-1} and C–S stretch vibration corresponding at 646 cm^{-1} shifts slightly because of the adsorption of Fe^{3+} ions onto the surface of the MQDs.[24] This adsorption slightly alters the local environment of the Mo–S bonds, reflected in the FTIR spectra. The emergence of new peaks at 632, 482, and 470 cm^{-1} further confirms the presence of Fe^{3+} ions on the surface of the MQDs, as these peaks

correspond to the formation of surface-bound complexes involving Fe^{3+} ions.[40–42] These results collectively demonstrate that Fe^{3+} ions are adsorbed onto the surface of MQDs, interacting with various functional groups, leading to the quenching of fluorescence and enabling the detection of Fe^{3+} ions through the observed changes in the FTIR spectra. A similar trend was evident in the UV-Vis spectra obtained after the introduction of Fe^{3+} ions to the MQDs (refer to Fig. S12 in the ESI†). The presence of Fe^{3+} ions induced a shift in the peak of the MQDs around 255 nm, accompanied by the emergence of an additional band around 350 nm, thereby confirming the formation of these supplementary ferric complexes.[45] These complexes are non-fluorescent in their natural state. Consequently, the underlying mechanism primarily relied on the static quenching of fluorescence of MQDs, wherein the fluorescence is reduced in the presence of Fe^{3+} ions.[46]

Additionally, XPS analysis of MQDs was conducted both before and after the detection of Fe^{3+} ions to explore the nature of their interaction. The XPS data confirmed the presence of Mo and S elements in the MQDs (Fig. 8(a)). The C 1s spectrum displayed a characteristic C=C/C–C peak at 284.9 eV (Fig. 8(b)). In the Mo 3d spectrum, two primary peaks at 228.7 eV (Mo $3d_{5/2}$) and 232.0 eV (Mo $3d_{3/2}$) correspond to the Mo(IV) oxidation state, with additional peaks at 236.5 and 233.2 eV indicating Mo(VI) state. The peak at 225.9 eV represents the S 2s state (Fig. 8(c)). The peaks at 162.6 and 161.7 eV correspond to the S $2P_{1/2}$ and S $2P_{3/2}$, respectively (Fig. 8(d)). No additional peaks were observed on comparing the XPS spectra of bare MQDs and MQDs after the addition of Fe^{3+} ions (Fig. 8(a)). The peak positions for Mo and S remained unchanged (Table S5†), suggesting that the interaction between MQDs and Fe^{3+} ions is primarily physical adsorption rather than chemical bonding. The observed reduction in peak intensity following Fe^{3+} adsorption further supports a static interaction, indicating that the chemical state of the MQDs remains unaltered by their interaction with Fe^{3+} ions.

Table 1 presents a comparison of the obtained data with reported literature on MoS_2 QDs for ion sensing and cell viability. Compared to the earlier reports, where most of the MoS_2 QDs were synthesized by the hydrothermal method, our different approach of microwave synthesis of MQDs has led to the generation of much smaller QDs with less polydispersity (1.9 ± 0.7 nm). These MQDs not only have a better quantum yield of ~9% but also have superior Fe^{3+} ion sensitivity with the LOD value as low as 27.61 ± 0.25 nM compared to the sensitivity of a range of a few μm in other QDs synthesized in Table 1. This Fe^{3+} fluorescent MQDs approach aspires to be a robust, practical, and effective Fe^{3+} detection technique. A Fe^{3+} detection system with a fast response time and stable fluorescence intensity after a response is essential for accurate sensing, as real-time monitoring is crucial for a variety of sensing applications. Our approach, therefore, promises potential for real-time Fe^{3+} monitoring in aqueous media because of its remarkable fluorescence stability, biocompatibility, and low LOD value.

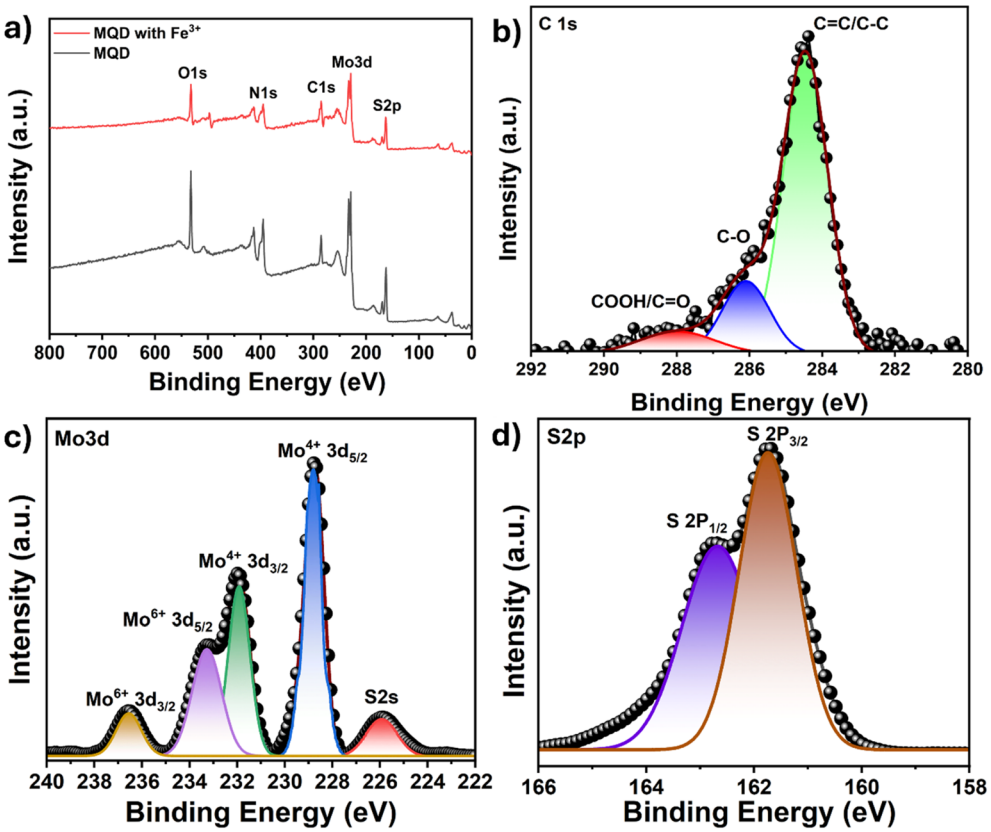

Fig. 8 (a) XPS survey spectra of MQD before and after Fe^{3+} ion detection, and high-resolution XPS spectra of (b) C 1s, (c) Mo 3d, and (d) S 2p.

Table 1 Literature comparison of MoS_2 QDs for Fe^{3+} ion detection system and cell viability studies

S. No.	Detection QD and size	Excitation and emission wavelength	QY	Ion detected and LOD	Cell viability (%) and concentration	Ref.
1	MoS_2 (3.7 nm)	Ex: 330 nm, Em: 450 nm	2.28%	2.06 μM, Fe^{3+} ions	—	41
2	MoS_2 (4.4 nm)	Ex: 360 nm, Em: 428 nm	5%	Fe^{3+}/Al^{3+} ions	Hela cell line, viability: 80%, conc: 100 μg mL^{-1}	47
3	MoS_2 (4.67 nm)	Ex: 310 nm, Em: 410 nm	6%	1 μmol L^{-1}, Fe^{3+} ions	—	38
4	N doped MoS_2 (3 nm)	Ex: 330 nm, Em: 400 nm	—	11 μM, Fe^{3+} ions	—	48
5	MoS_2 (6.2 nm)	Ex: 340 nm, Em: 427 nm	19%	0.4 μmol L^{-1}, Fe^{3+} ions	—	49
6	MoS_2 QD (3.0 nm)	Ex: 300 nm, Em: 400 nm	5.3%	0.24 μM, Fe^{3+} ions	—	40
7	MoS_2 (3.5 nm)	Ex: 330 nm, Em: 405 nm	6.5%	0.3 μM, hydroquinone	Hela cell line, viability: 85%, conc: 200 μg mL^{-1}	31
8	MoS_2 QD, **1.86 ± 0.69 nm**	Ex: 315 nm, Em: 405 nm and 530 nm	**8.95 ± 0.019%**	**27.61 nM**, Fe^{3+} ions	SK-BR-3 and RPE-1 cell line, viability: **80%/76%**, Conc: **1000 μg mL^{-1}**	This study

4. Conclusions

MoS_2 quantum dots were successfully synthesized using a microwave-assisted method. The size and morphology were characterized by TEM and AFM, where the average diameter is calculated to be 1.9 ± 0.7 nm, which agrees well with the height profiling of the MQDs. The absorbance studies verify the characteristic transitions of MoS_2 having absorption humps ranging from 260 to 280 nm and 300 nm to 330 nm with a band gap of 3.6 ± 0.1 eV. The fluorescence emission studies reveal that the dominant blue (and some green) emissions were recorded under the excitation of 315 nm wavelength. The absolute quantum yield was determined to be 8.95 ± 0.019%. The MQDs showed excellent stability with time-dependent fluorescence and repeated quenching cycles. The applicability of the MQDs was determined at different pH systems and media systems, demonstrating the robustness of the synthesized MQDs. The *in vitro* toxicity investigations demonstrated the biocompatibility of MQDs, exhibiting around 80% cell survival even at elevated concentrations of 1000 mg L^{-1}. In both cancerous and non-cancerous cell lines, the confocal-based cellular imaging demonstrated substantial uptake of the MQDs and vibrant blue and green fluorescence throughout the cells. Additionally, the MQDs demonstrated strong selectivity for Fe^{3+} ions among all other heavy metal ions, and their detection limit was recorded to be 27.61 ± 0.25 nM. Our synthesized MQDs-based Fe^{3+} detection method has excellent fluorescence stability, robustness, and efficient Fe^{3+} detection with low LOD values. Further, MQDs offer enhanced cell viability, high biocompatibility, and dual-channel imaging properties. Finally, our study demonstrated that microwave-synthesized MoS_2 quantum dots effectively detect Fe^{3+} in biological media, with recovery rates of >97% in PBS and >98% in SBF and an RSD within 3%, indicating excellent precision. Due to a combination of such remarkable properties, these QDs offer the potential to be utilized in the diagnostics of diseases that have a deficiency or excess of Fe^{3+}.

Data availability

The data supporting this article have been included as part of the ESI.†

Author contributions

VT: conceptualization, data curation, investigation, methodology, validation, writing – original draft. SS: conceptualization, visualization, data curation, writing – original draft. SKM: resources, validation, writing – review & editing. RB: conceptualization, funding acquisition, project administration, validation, resources, supervision, writing – review & editing.

Conflicts of interest

There are no conflicts to declare.

Acknowledgements

Vishakha Takhar thanks the Prime Minister's Research Fellowship, Govt. of India (MIS/IITGN/PMRF/RB/2022-23/026)

for support. We also thank the Central Instrumentation Facility at IIT Gandhinagar for facilitating several measurements.

References

1 G. Paramasivam, V. V. Palem, S. Meenakshy, L. K. Suresh, M. Gangopadhyay, S. Antherjanam and A. K. Sundramoorthy, *Colloids Surf., B*, 2024, 114032.
2 A. Singh, S. S. Shah, C. Sharma, V. Gupta, A. K. Sundramoorthy, P. Kumar and S. Arya, *J. Environ. Chem. Eng.*, 2024, 113032.
3 K. H. Vardhan, P. S. Kumar and R. C. Panda, *J. Mol. Liq.*, 2019, **290**, 111197.
4 A. K. Sundramoorthy, B. S. Premkumar and S. Gunasekaran, *ACS Sens.*, 2016, **1**, 151–157.
5 G. J. Kontoghiorghes, *Int. J. Mol. Sci.*, 2023, **24**, 12928.
6 X. Bao, X. Cao, X. Nie, Y. Xu, W. Guo, B. Zhou, L. Zhang, H. Liao and T. Pang, *Sens. Actuators, B*, 2015, **208**, 54–56.
7 A. M. Senol and E. Bozkurt, *Microchem. J.*, 2020, **159**, 105357.
8 K. D. Pagana, T. J. Pagana and T. N. Pagana, *Mosby's Diagnostic & Laboratory Test Reference*, Elsevier, St. Louis, Mo, 14th edn, 2019.
9 J. E. Cassat and E. P. Skaar, *Cell Host Microbe*, 2013, **13**, 509–519.
10 Q. Ding, C. Li, H. Wang, C. Xu and H. Kuang, *Chem. Commun.*, 2021, **57**, 7215–7231.
11 P. Rasin, V. Manakkadan, V. N. Vadakkedathu Palakkeezhillam, J. Haribabu, C. Echeverria and A. Sreekanth, *ACS Omega*, 2022, **7**, 33248–33257.
12 J. Hu, F. Liu, Y. Chen, G. Shangguan and H. Ju, *ACS Sens.*, 2021, **6**, 3517–3535.
13 F. Yin, F. Wang, C. Fan, X. Zuo and Q. Li, *View*, 2021, **2**, 20200038.
14 O. Sadak, R. Hackney, A. K. Sundramoorthy, G. Yilmaz and S. Gunasekaran, *Environ. Nanotechnol. Monit. Manag.*, 2020, **14**, 100380; H. Huang, L. Liao, X. Xu, M. Zou, F. Liu and N. Li, *Talanta*, 2013, **117**, 152–157.
15 A. M. Derfus, W. C. Chan and S. N. Bhatia, *Nano Lett.*, 2004, **4**, 11–18.
16 Y. Xu, X. Wang, W. L. Zhang, F. Lv and S. Guo, *Chem. Soc. Rev.*, 2018, **47**, 586–625.
17 V. Takhar, S. Singh, S. Dhakar, M. R. A. Qureshi, S. Sharma, S. K. Misra and R. Banerjee, *ChemCatChem*, 2024, e202400684.
18 Y. Guo and J. Li, *Mater. Sci. Eng. C*, 2020, **109**, 110511.
19 J. Sun and X. Meng, *ACS Appl. Nano Mater.*, 2021, **4**, 11413–11427.
20 M. S. Ali, N. Bhunia, M. S. Ali, S. Karmakar, P. Mukherjee and D. Chattopadhyay, *Chem. Phys. Lett.*, 2023, **825**, 140574.
21 S. Lambora and A. Bhardwaj, *ACS Appl. Nano Mater.*, 2024, **7**(1), 163–169.
22 Á. Coogan and Y. K. Gun'ko, *Mater. Adv.*, 2021, **2**, 146–164.
23 R. Mahle, P. Kumbhakar, D. Nayar, T. N. Narayanan, K. K. Sadasivuni, C. S. Tiwary and R. Banerjee, *Dalton Trans.*, 2021, **50**(40), 14062–14080.
24 R. Mahle, D. Mandal, P. Kumbhakar, A. Chandra, C. S. Tiwary and R. Banerjee, *Biomater. Sci.*, 2021, **9**(1), 157–166.
25 G. Yang and S. J. Park, *Mater*, 2019, **12**, 1177.
26 S. Santra, M. S. Ali, S. Karmakar and D. Chattopadhyay, *Mater. Today Sustain.*, 2023, 100659.
27 S. Singh, S. H. Nannuri, S. D. George, S. Chakraborty, A. Sharma and S. K. Misra, *J. Environ. Chem. Eng.*, 2021, **9**, 105813.
28 S. H. Nannuri, S. Singh, S. Chidangil and S. D. George, *Mater. Technol.*, 2022, **37**, 2893–2906.
29 S. Singh, V. Takhar, S. H. Nannuri, S. D. George, R. Banerjee and S. K. Misra, *ACS Appl. Nano Mater.*, 2023, **6**, 10441–10452.
30 N. H. Attanayake, A. C. Thenuwara, A. Patra, Y. V. Aulin, T. M. Tran, H. Chakraborty and D. R. Strongin, *ACS Energy Lett.*, 2017, **3**(1), 7–13.
31 L. Li, Z. Guo, S. Wang, D. Li, X. Hou, F. Wang, Y. Yang and X. Yang, *Anal. Methods*, 2019, **11**, 3307–3313.
32 D. M. Vidyadharan, N. Pullanjiyot, B. Ninnora Meethal, S. S. Kanakkillam, S. Sadasivan and S. Swaminathan, *Appl. Nanosci.*, 2019, **9**, 435–445.
33 S. Singh, V. S. A. Varri, K. Parekh and S. K. Misra, *Colloids Surf., B*, 2023, **232**, 113579.
34 A. Arathi, X. Joseph, V. Akhil and P. V. Mohanan, *Colloids Surf., B*, 2022, **211**, 112300.
35 D. V. Vishnevetskii, A. R. Mekhtiev, T. V. Perevozova, A. I. Ivanova, D. V. Averkin, S. D. Khizhnyak and P. M. Pakhomov, *Soft Matter*, 2022, **18**, 3031–3040.
36 A. Kapur, S. H. Medina, W. Wang, G. Palui, X. Ji, J. P. Schneider and H. Mattoussi, *ACS Omega*, 2018, **3**, 17164–17172.
37 I. C. Carvalho, A. A. Mansur, S. M. Carvalho, R. M. Florentino and H. S. Mansur, *Int. J. Biol. Macromol.*, 2019, **133**, 739–753.
38 J. Ma, H. Yu, X. Jiang, Z. Luo and Y. Zheng, *Sens. Actuators, B*, 2019, **281**, 989–997.
39 A. Srinivasan and N. Rajendran, *RSC Adv.*, 2015, **5**, 26007–26016.
40 M. S. Ali, M. S. Ali, N. Bhunia, A. Mallik, K. Dutta, S. Karmakar, P. Mukherjee and D. Chattopadhyay, *J. Phys. Chem. Solids*, 2023, **176**, 111261.
41 H. Mishra, V. K. Singh, R. Ali, K. Vikram, J. Singh, A. Misra, H. Mishra and A. Srivastava, *Monatsh. Chem.*, 2020, **151**, 729–741.
42 N. Dhenadhayalan, T. W. Lin, H. L. Lee and K. C. Lin, *ACS Appl. Nano Mater.*, 2018, **1**, 3453–3463.
43 S. Bhatt, M. Bhatt, A. Kumar, G. Vyas, T. Gajaria and P. Paul, *Colloids Surf., B*, 2018, **167**, 126–133.
44 X. Zhu, Z. Zhang, Z. Xue, C. Huang, Y. Shan, C. Liu, X. Qin, W. Yang, X. Chen and T. Wang, *Anal. Chem.*, 2017, **89**, 12054–12058.
45 Y. Zhang, F. Li, C. He, H. Ma, Y. Feng, Y. Zhang and M. Zhang, *Sens. Actuators, B*, 2018, **255**, 1878–1883.
46 N. Arjmandi, W. Van Roy, L. Lagae and G. Borghs, *Anal. Chem.*, 2012, **84**, 8490–8496.
47 Q. Wu, X. Wang, Y. Jiang, W. Sun, C. Wang, M. Yang and C. Zhang, *ChemistrySelect*, 2018, **3**, 2326–2331.
48 Y. Zhang, S. Zhou, H. Liu, X. Tang, H. Zhou and H. Cai, *Microchem. J.*, 2021, **169**, 106553.
49 L. Ruan, Y. Zhao, Z. Chen, W. Zeng, S. Wang, D. Liang and J. Zhao, *Appl. Surf. Sci.*, 2020, **528**, 146811.

